RSC Advances

PAPER

View Article Online
View Journal | View Issue

Cite this: *RSC Adv.*, 2018, **8**, 27516

Regenerable g-C_3N_4–chitosan beads with enhanced photocatalytic activity and stability

Chaocheng Zhao, †* Qingyun Yan,† Shuaijun Wang, Pei Dong and Liang Zhang

In this study, a series of regenerable graphitic carbon nitride–chitosan (g-C_3N_4–CS) beads were successfully synthesized *via* the blend crosslinking method. The prepared beads were characterized by scanning electron microscopy (SEM), thermogravimetric analysis (TGA), X-ray diffraction (XRD), Fourier transform infrared spectroscopy (FT-IR), diffuse reflectance spectroscopy (DRS), photoluminescence (PL) spectroscopy, and X-ray photoelectron spectroscopy (XPS). The structural characterization results indicate that the g-C_3N_4 granules were uniformly distributed on the surface of the chitosan matrix, and the structures of g-C_3N_4 and CS are maintained. In addition, the prepared g-C_3N_4–CS beads exhibited efficient MB degradation and stability. The optimum photocatalytic activity of our synthesized g-C_3N_4–CS beads was higher than that of the bulk g-C_3N_4 by a factor of 1.78 for MB. The improved photocatalytic activity was predominantly attributed to the synergistic effect between *in situ* adsorption and photocatalytic degradation. In addition, the reacted g-C_3N_4–CS beads can be regenerated by merely adding sodium hydroxide and hydrogen peroxide. Additionally, the regenerated g-C_3N_4–CS beads exhibit excellent stability after four runs, while the mass loss is less than 10%. This work might provide guidance for the design and fabrication of easily regenerated g-C_3N_4-based photocatalysts for environmental purification.

Received 20th May 2018
Accepted 25th July 2018

DOI: 10.1039/c8ra04293d

rsc.li/rsc-advances

1. Introduction

Photocatalytic technology can utilize the inexhaustible solar energy, which is broadly applicable in the field of energy and environmental protection and has been widely applied to energy production.[1–8] Semiconductors, especially TiO_2,[9–11] have been widely studied as photocatalysts, which have advantages including chemical stability, nontoxicity, no secondary pollution and low costs.[12–16] They also have disadvantages based on in-depth research, which are their excitability only by ultraviolet light, wide bandgap energy, low photocatalytic efficiency and the electrons and holes being prone to recombination.[17–23] New materials should be explored to compensate for these shortcomings.

Recently, graphitic carbon nitride (g-C_3N_4) has attracted attention as a metal-free catalyst.[24–28] Compared with traditional inorganic semiconductors, g-C_3N_4 possesses a narrow band gap of ~2.7 eV,[29–32] good resistance to thermal and chemical damage (acid, base and organic solvent),[4,33] and visible absorption at approximately 450–460 nm.[34–36] Nevertheless, in the stability experiment, there is a problem of mass loss due to the powdered g-C_3N_4.[37–39] In addition, g-C_3N_4 has general adsorption properties on account of the structure. As a natural alkaline cationic polymer, chitosan (CS) has excellent biocompatibility, nontoxicity, biodegradability and other advantages.[40] CS is a product of chitin deacetylated, containing a significant amount of amino and hydroxy groups in the molecule, which has excellent flocculation and adsorption characteristics. The CS has a chain-like structure that is easy to crystallize; and has a stable crystalline structure, that is insoluble in water, alkali and most organic solvents.[41–43]

In previously reported studies, Nishad *et al.*[44] prepared stable beads by using nano-TiO_2 and CS and exhibited full adsorption performance for niobium of the +3 and +5 oxidation states. Yang Limin *et al.*[45] prepared an easily regenerated TiO_2 impregnated CS adsorbent, and at the same time, absorbed the photosensitizing effect of TiO_2 to achieve the adsorption and degradation of pollutants. Inspired by previous work, if a suitable method can be used to combine g-C_3N_4 and CS to design an easily regenerated composite catalyst with good photocatalytic ability and adsorption capacity, while reducing mass loss to improve the stability and utilization in cycle experiments, it will effectively improve the g-C_3N_4-based catalyst. The catalytic efficiency meets the requirements for practical application. To the best of our knowledge, few studies have combined g-C_3N_4 and CS to date.

Herein, in this study, g-C_3N_4–CS beads were first synthesized *via* the blend crosslinking method. The effect of the ratio between the g-C_3N_4 and CS to the *in situ* adsorption and photocatalytic activity of the products was investigated. SEM, XRD,

State Key Laboratory of Petroleum Pollution Control, China University of Petroleum (East China), Qingdao, 266580, PR China. E-mail: zhaochch0821@163.com
† These authors contributed equally to this work.

FT-IR, DRS, PL and XPS measurements were performed to determine the morphology and phase change. Photocatalytic decomposition of methylene blue (MB) was carried out to evaluate the photocatalytic properties of the g-C_3N_4–CS beads. The results show that there is an optimal ratio between g-C_3N_4 and CS to coordinate *in situ* adsorption and photocatalytic activity to achieve the best level.

2. Material and methods

2.1 Material and reagents

Melamine, chitosan (CS, 85% deacetylation), epichlorohydrin, sodium hydroxide, anhydrous acetic acid, methylene blue (MB), isopropanol (IPA), triethanolamine (TEOA), and *p*-benzoquinone (BQ) were purchased from Sinopharm Chemical Reagent Company (China). All chemicals were of analytical grade and used without any further purification unless otherwise mentioned.

2.2 Preparation of regenerable g-C_3N_4–CS-*x* beads

2.2.1 Preparation of g-C_3N_4. Graphitic carbon nitride was prepared *via* the thermal polycondensation of melamine. Melamine was put into an alumina crucible with a cover and calcined in air at 550 °C for 2 h with a ramping rate of 5°C min^{-1} in a muffle furnace, followed by naturally cooling to room temperature. Finally, the harvested samples were crushed in an agate mortar and put into the fine for further use.

2.2.2 Preparation of the regenerable g-C_3N_4–CS-*x* beads. Regenerable g-C_3N_4–CS-*x* beads samples were prepared *via* the blend crosslinking method as follows: the CS powder was dissolved to a certain concentration of the acetic acid solution and stirred until the CS completely dissolved. The prepared g-C_3N_4 powder was added to the homogeneous colloidal solution. The cross-linking agent epichlorohydrin (2 mL) was subsequently added, reacting for 60 min at room temperature after sonicating for 60 min. The homogeneous colloidal solution was added as drops into the 1% sodium hydroxide solution under constant stirring. The drops were isolated and coagulated to form guttulate beads. Then, the beads were separated and washed several times with distilled water until the filtrate was measured to be approximately pH = 7; and were denoted as g-C_3N_4–CS-*x*, where the *x* value represent the CS and the g-C_3N_4 ratio ($x = 1$, 2, 3, and 4). The final g-C_3N_4–CS-*x* beads within a certain size range (1 ± 0.1 mm) were obtained by drying at 60 °C in a vacuum drying oven for 5 h. It is worth mentioning that the needle size determines the bead size.

The crosslinking process of the g-C_3N_4–CS-*x* samples are shown in Fig. 1. g-C_3N_4 with a heptazine ring as a structural unit was calcined at 550 °C by the melamine precursor. The CS molecules interact with each other *via* epichlorohydrin to form a network structure, which crosslinks with g-C_3N_4 to form g-C_3N_4–CS beads.

2.2.3 Regeneration of the g-C_3N_4–CS-*x* beads. The regeneration of the g-C_3N_4–CS-*x* beads was carried out under a visible-light irradiation reaction which has a 300 W Xe lamp with a 420 nm cut-off filter as the light source. After the photocatalytic measurements, the g-C_3N_4–CS-*x* beads were filtered and placed in a 0.5 mol L^{-1} sodium hydroxide solution. A total of 5 μL H_2O_2 was added, and then, the mixed system was magnetically stirred in the light for 3 h. Finally, the beads were separated and washed several times with distilled water until the filtrate was measured to be approximately neutral pH, and the g-C_3N_4–CS-*x* beads were regenerated after air-drying at 60 °C for 5 h. This process was repeated five times to measure the stabilities of the beads.

2.3 Characterization

The thermogravimetric analysis (TGA) was conducted with a TGA Q500 (TA Instruments) under N_2 flow, from 50 to 780 °C, with a heating rate of 10 °C min^{-1}. The surface texture of the

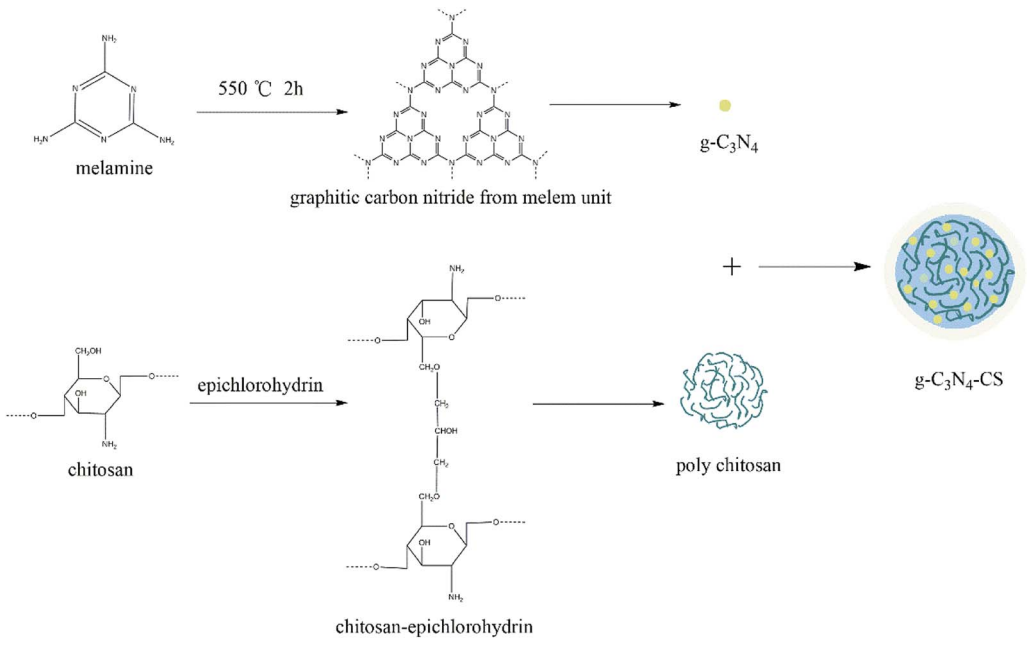

Fig. 1 The crosslinking process of the g-C_3N_4–CS-*x* samples.

samples was investigated by emission scanning electron microscopy (SEM) (S-4800). The energy dispersive X-ray spectrum (EDX) was obtained from an attached Oxford Link ISIS energy-dispersive spectrometer fixed on a JEM-2010 electron microscope. The powder X-ray diffraction (XRD) of the g-C_3N_4–CS-*x* beads was measured by a Bruker D8 Advance diffractometer with Cu Kα1 monochromatized radiation (λ = 1.5406 Å). The FT-IR spectrum in the range of 4000–400 cm^{-1} was recorded by using the KBr pellet technique. The diffuse reflectance spectroscopy (DRS) experiments were measured *via* a PerkinElmer spectrophotometer, which was equipped with an integrating sphere assembly with a nominal resolution of 1 nm using $BaSO_4$ as a reference. The photoluminescence (PL) spectrum was collected by a Hitachi F-7000 (Japan) spectrophotometer. The X-ray photoelectron spectroscopy (XPS) data were carried out on a Thermo ESCALAB250 instrument using a monochromatized Al Kα line source. Solid-state ^{13}C Nuclear Magnetic Resonance (NMR) measurements were carried out on a Bruker Avance III spectrometer.

2.4 Photocatalytic test

The photocatalytic activity of the g-C_3N_4–CS-*x* beads was evaluated by the degree of degradation of the MB solution including a 100 mL MB solution (5 mg L^{-1}) and g-C_3N_4–CS-*x* (0.20 g). The reaction was performed in a photoreactor apparatus used to simulate sunlight (equipped with a 300 W xenon arc with a 420 nm cutoff filter) as a visible light source. The temperature of the reactant solution was kept at room temperature *via* a flow of cooling water. Before irradiation, the suspension was magnetically stirred in the dark for 60 min to achieve adsorption/desorption equilibrium. To quantify MB, a small sample (2.00 mL) of this suspension was taken out at given intervals and the absorbance of the removed filtrate was measured at 664 nm with an ultraviolet-visible spectrophotometer.

3. Results and discussion

3.1 Characterization of the g-C_3N_4–CS-*x* beads

Thermogravimetric analysis was measured to investigate the thermal stability of the g-C_3N_4–CS-*x* beads. Fig. 2 shows the TGA patterns of the g-C_3N_4, the CS and the g-C_3N_4–CS-3. The maximum rate of weight loss for g-C_3N_4 is observed at approximately 600–750 °C,[46] which is caused by the decomposition of carbon nitride.[47] The initial water loss for the CS is observed at near 260 °C, meaning the water adsorbed on the surface of the material was steamed. Due to the decomposition of CS, the hydroxyl and C–O bonds in the molecule are rapidly destroyed, and accompanied with a large loss of hydrogen, oxygen, and small amounts of carbon, the CS begins to decompose at 260 °C, the weight gradually decrease as the temperature increases, and there are no residual until 750 °C. The weight loss of the g-C_3N_4–CS-3 beads is observed before 260 °C, which can be attributed to the water loss, and the weight loss from 260 to 750 °C; is due to the CS decomposition; therefore, the g-C_3N_4 starts decomposing at 600 °C.

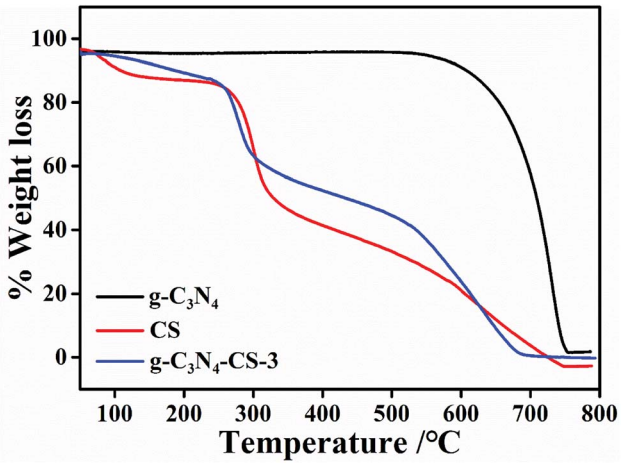

Fig. 2 TGA patterns of the g-C_3N_4, the CS and the g-C_3N_4–CS-3 samples.

Fig. 3 presents the XRD patterns of the g-C_3N_4, the CS and the g-C_3N_4–CS-3. It can be seen that the CS has two distinct diffraction peaks at 11° and 20°,[40] meaning the CS has a specific microcrystalline structure. For the g-C_3N_4, two characteristic peaks at 13.1° and 27.4° are observed,[24,25] corresponding to the (002) and (100) diffraction of the g-C_3N_4 structure. It is clear that the g-C_3N_4–CS-3 beads have two peaks at 20° and 27.4°, indicating that the g-C_3N_4 and CS were successfully assembled, among them, the diffraction peak at 2θ = 20° belongs to the microcrystalline structure of CS, and the diffraction peak at 2θ = 27.4° belongs to the inter-layer stacking of g-C_3N_4, corresponding to the (002) crystal plane.

The texture of g-C_3N_4–CS-3 can be observed *via* SEM images presented in Fig. 4, and the yellow region in Fig. 4a is appropriately enlarged and shown in Fig. 4b. It is clear that the CS has a compact structure and smooth surface,[48] and many granules are observed (Fig. 4a) which is further determined to be the g-C_3N_4 (Fig. 4b). From Fig. 4b, it can be seen that the g-C_3N_4 displays a typical wrinkled morphology, with few mesopore caused by structural collapse.

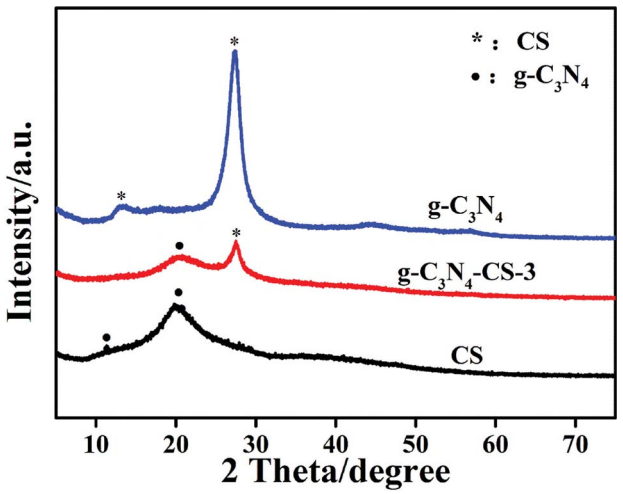

Fig. 3 XRD patterns of the g-C_3N_4, the CS and the g-C_3N_4–CS-3 samples.

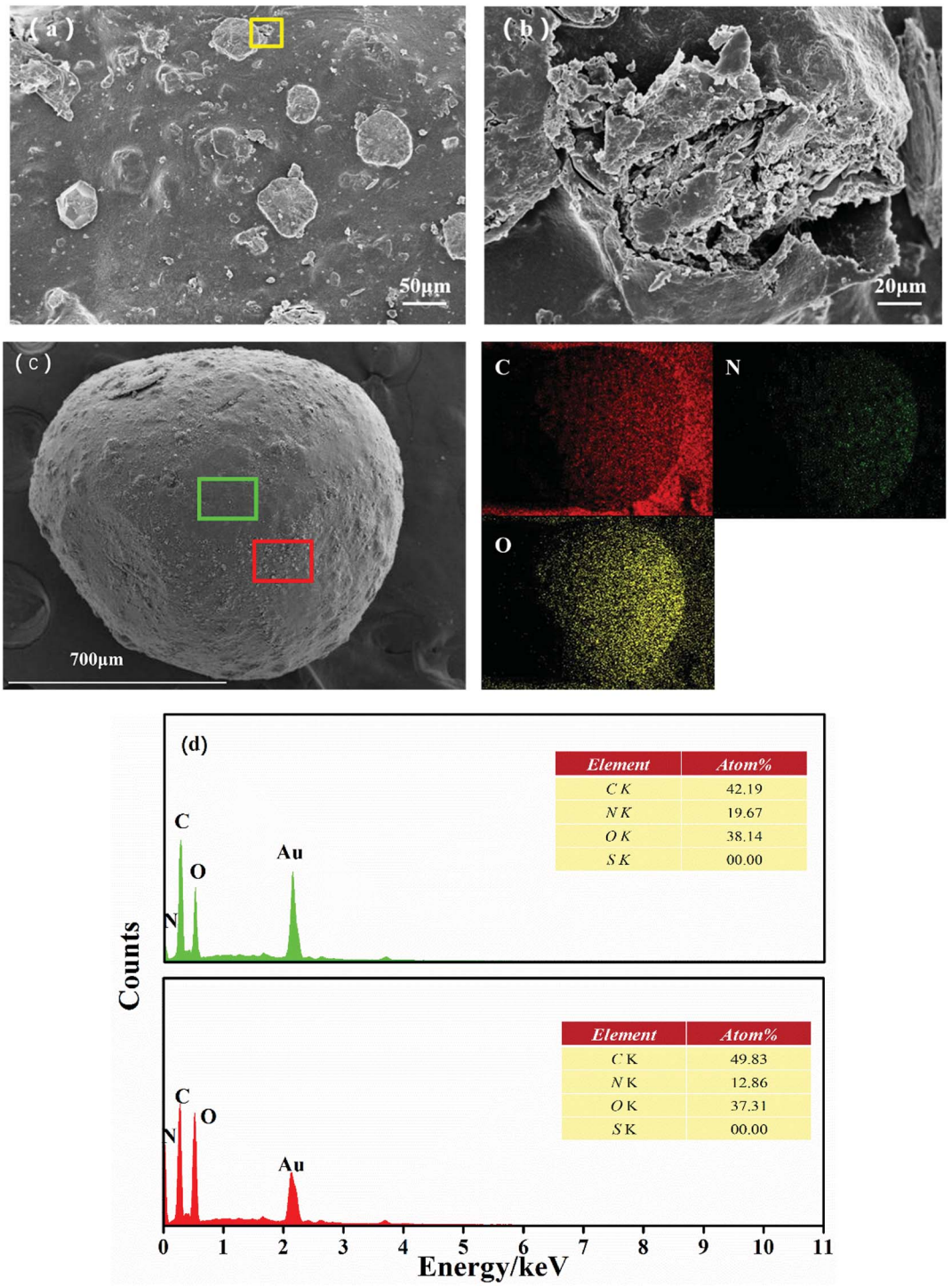

Fig. 4 SEM images (a and b) of the g-C_3N_4–CS-3 samples, EDX elemental mapping (c) and EDX spectra of the rectangle region indicated by green border (upper) and red border (d) for g-C_3N_4–CS-3.

The elemental mapping indicated that the distribution of C, N, and O elements were relatively homogeneous in g-C_3N_4–CS-3 (Fig. 4c), breakpoints can be seen in C elemental mapping, and relatively concentrated points can be seen in N elemental mapping, which may be due to different C and N content of CS and g-C_3N_4. And the EDX measurement confirmed the co-existence of C, N, and O elements in g-C_3N_4–CS-3 (Fig. 4d). The granule is further determined to be the aggregation of g-C_3N_4 nanoparticles, based on the high N peak in the EDX spectrum at the spot.

Elemental analysis is an effective method to determine the ratio between g-C_3N_4 and CS. Table 1 shows that the content of N element in g-C_3N_4–CS-3 is increased, suggesting that g-C_3N_4 is successfully embedded in the CS matrix. Considering

Table 1 Elemental analysis of the g-C_3N_4, the CS and the g-C_3N_4–CS-3 samples

Sample	C (wt%)	N (wt%)	H (wt%)	C/N (atomic ratio)
g-C_3N_4	34.43	61.43	1.78	0.65
CS	37.94	7.03	7.29	6.30
g-C_3N_4–CS-3	34.74	7.92	6.30	5.12

TGA, we can conclude that the ratio of g-C_3N_4 to CS is approximately 21.5 wt%, where the theoretical ratio of chitosan to g-C_3N_4 during the preparation was 25 wt%.

The FT-IR spectra of the g-C_3N_4, the CS and the g-C_3N_4–CS-3 samples are presented in Fig. 5. The characteristic peaks of CS and g-C_3N_4 were observed in the g-C_3N_4–CS-3 sample. For CS, typical strong absorption peaks of alcoholic hydroxyl groups C–O stretching vibration at 1024 and 1068 cm^{-1} are observed.[40] The broadband from 3000 to 3600 cm^{-1}, corresponds to N–H breathing modes, which is likely to indicate the presence of surface N–H or the presence of NH_2. A series of peaks in the region from 1200 to 1600 cm^{-1} were caused by aromatic CN heterocycle stretching vibration. Additionally, the typical bands at 810 cm^{-1} originate from the breathing vibration of the heptazine units. Combined with XRD analysis, g-C_3N_4 has successfully combined with CS.

DRS spectroscopy analyzed the optical absorption properties of the prepared samples. The light absorption edge of the g-C_3N_4 material is approximately 480 nm (Fig. 6); the absorption edge slightly shifts to 450 nm after doping CS, because CS has no light absorption. However, g-C_3N_4–CS-3 still has fair photocatalytic properties even though the absorption decreased.

Photoluminescence emission spectra with an excitation wavelength at 320 nm were used to characterize the efficiency of the charge immigration and separation in the samples. The lower the PL density, the better the termination of the photogenerated charge carriers. As shown in Fig. 7, the CS has

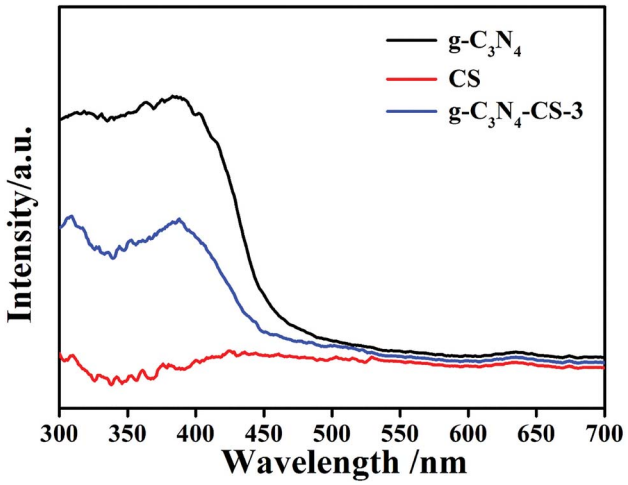

Fig. 6 DRS spectra of the g-C_3N_4, the CS and the g-C_3N_4–CS-3 samples.

negligible PL density. The PL density of g-C_3N_4–CS-3 is appreciably lower than that of g-C_3N_4, it may be the incorporation of CS that leads to a decrease in the dispersion density of g-C_3N_4, resulting in a reduction in the density.

The chemical composition and chemical states of the g-C_3N_4–CS-3 samples were examined by XPS measurements. The survey spectra reveal that the elements of C, N and O exist in the samples. The element O may come from the CS and the absorbed H_2O and CO_2 on the surface of the g-C_3N_4–CS-3 (Fig. 8a). Three peaks were observed in the C 1s spectrum[37] (Fig. 8b); the peak at 288.1 eV was assigned to the sp^2 N–C=N in the N-containing aromatic ring, the 286.2 eV peak is identified as the sp^2-hybridized carbon in the C–N–C of g-C_3N_4 and the C–O bonds of CS,[49] and according to the literature, the 284.6 eV is ascribed to the sp^2 C–C bonds. The N 1s spectra (Fig. 8c) can be separated into four peaks at 398.4 eV, 399.1 eV, 399.6 eV, and 400.6 eV corresponding to the sp^2 C–N=C bonds, C–NH–C bonds, bridge N in the N–$(C)_3$ groups, and the sp^2-bonded N in

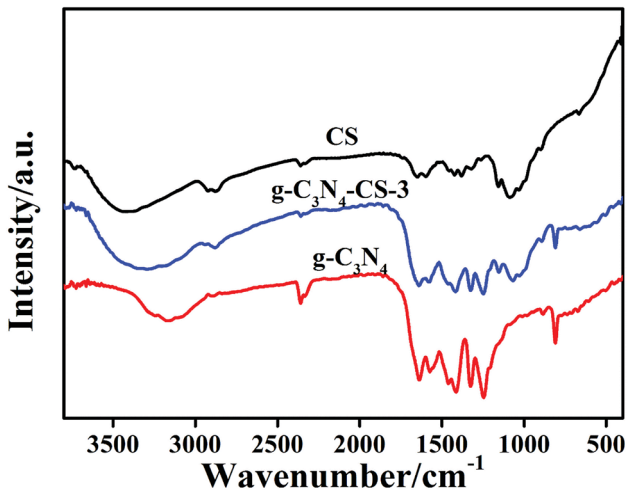

Fig. 5 FT-IR spectra of the g-C_3N_4, the CS and the g-C_3N_4–CS-3 samples.

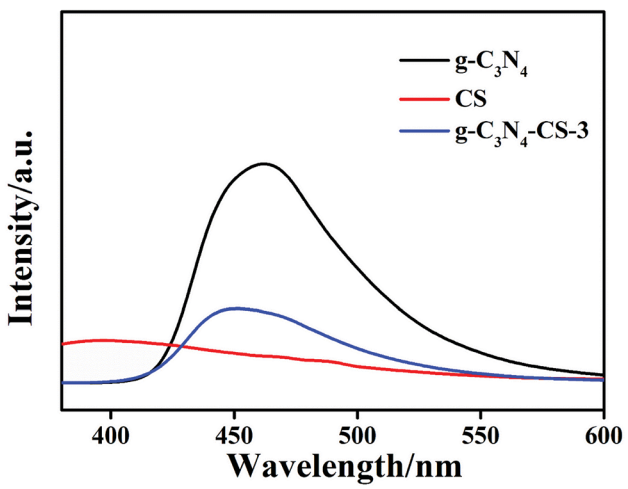

Fig. 7 PL spectra of the g-C_3N_4, the CS and the g-C_3N_4–CS-3 samples.

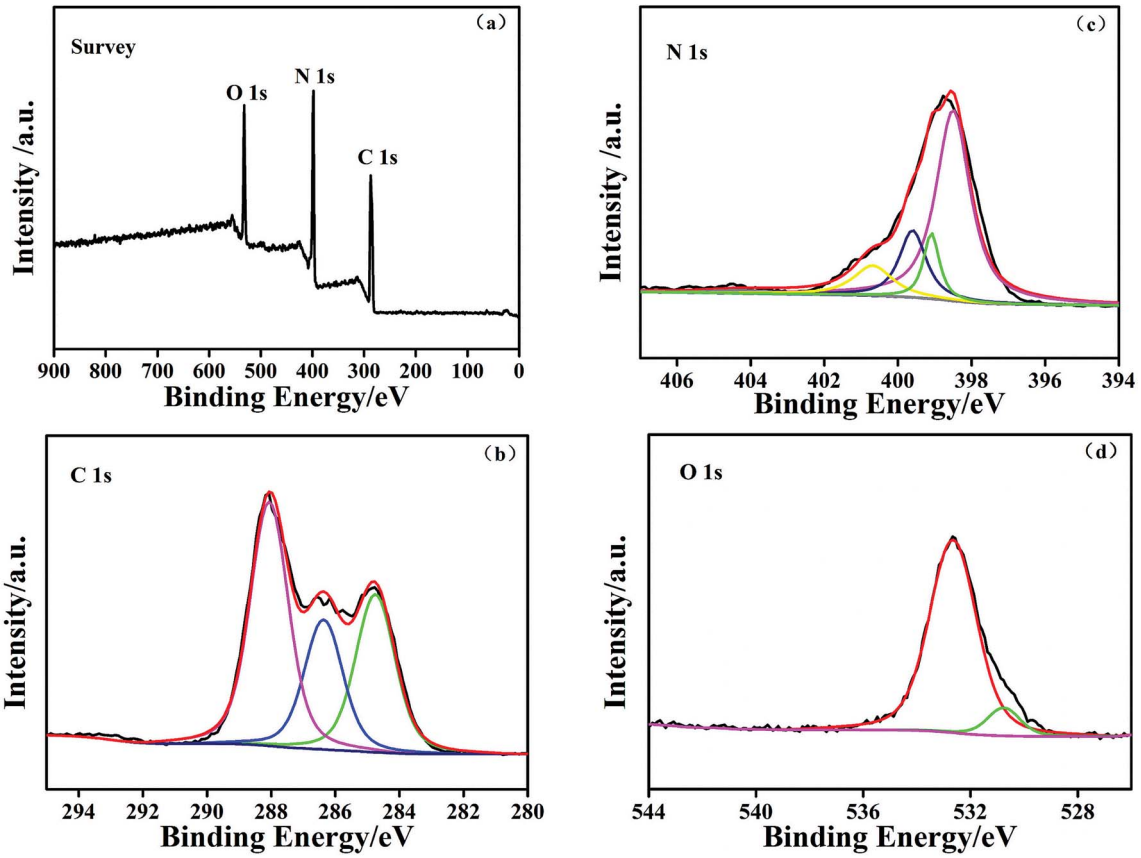

Fig. 8 The XPS of the g-C_3N_4–CS-3 samples for the (a) survey spectrum, (b) C 1s, (c) N 1s, and (d) O 1s.

the aromatic heterocyclic, respectively. The O 1s spectra (Fig. 8d) show two distinct peaks at approximately 530.8 eV and 532.6 eV. The 530.8 eV peak is identified as tertiary amine oxidative C═O or HN═C═O.[50] In addition, the peak at 532.6 eV originates from the water molecules adsorbed on the surface.

Solid-state NMR spectroscopy is one of the most powerful techniques for addressing issues of molecular structure, especially for insoluble or poorly materials. In the ^{13}C NMR spectra of g-C_3N_4–CS-3 (Fig. 9), two common signals centered at 154.2 and 162.3 ppm are assigned to CN_3 and CN_2NH_2 groups of g-C_3N_4 material, respectively. This indicated that the existence of g-C_3N_4 of the sample. And disappearance of the signal at 20.5, 53.3, 58.3, 71.5, 73.3, 80.1, and 101.2 ppm are assigned to CH_3, $OC(CH_2)_2$, $CHNH_2$, CO, CHOH, CHO–, OCHO– groups of chitosan–epichlorohydrin.

3.2 Photocatalytic activity

The photocatalytic activity of the samples was evaluated *via* the photodegradation of MB under visible light irradiation. Fig. 10 shows the photocatalytic results for MB degradation (start lighting at 0 min. The inset is the adsorption–desorption equilibrium curves showing that the systems get an adsorption–desorption equilibrium after 60 min in dark). The higher the CS mixing is, the higher the absorption; the adsorption effect covers the highlight of the photocatalytic performance when CS mixes too much (Fig. 10a). To balance the effects of adsorption and photocatalytic activity, we regard g-C_3N_4–CS-3 as the mixing ratio, which can appropriately improve the *in situ* adsorption, while maintaining the maximum impact of the photocatalytic performance.

The corresponding first-order-kinetic curves for the MB photodegradation over the g-C_3N_4 and g-C_3N_4–CS-*x* photocatalysts are shown in Fig. 10b. The experimental data correlate with the first-order reaction kinetic equation:

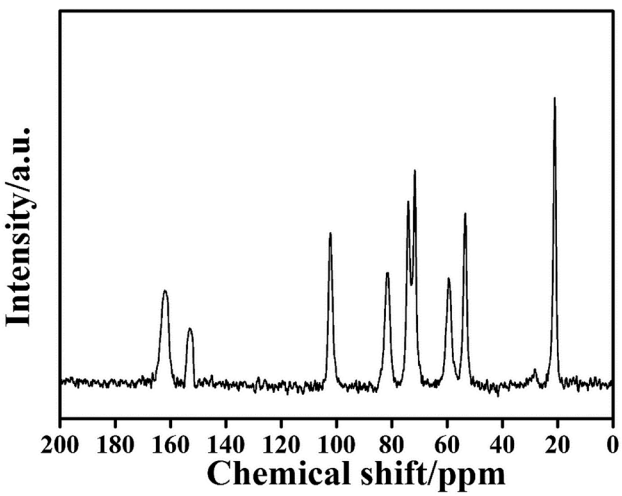

Fig. 9 Solid-state ^{13}C NMR of the g-C_3N_4–CS-3 samples.

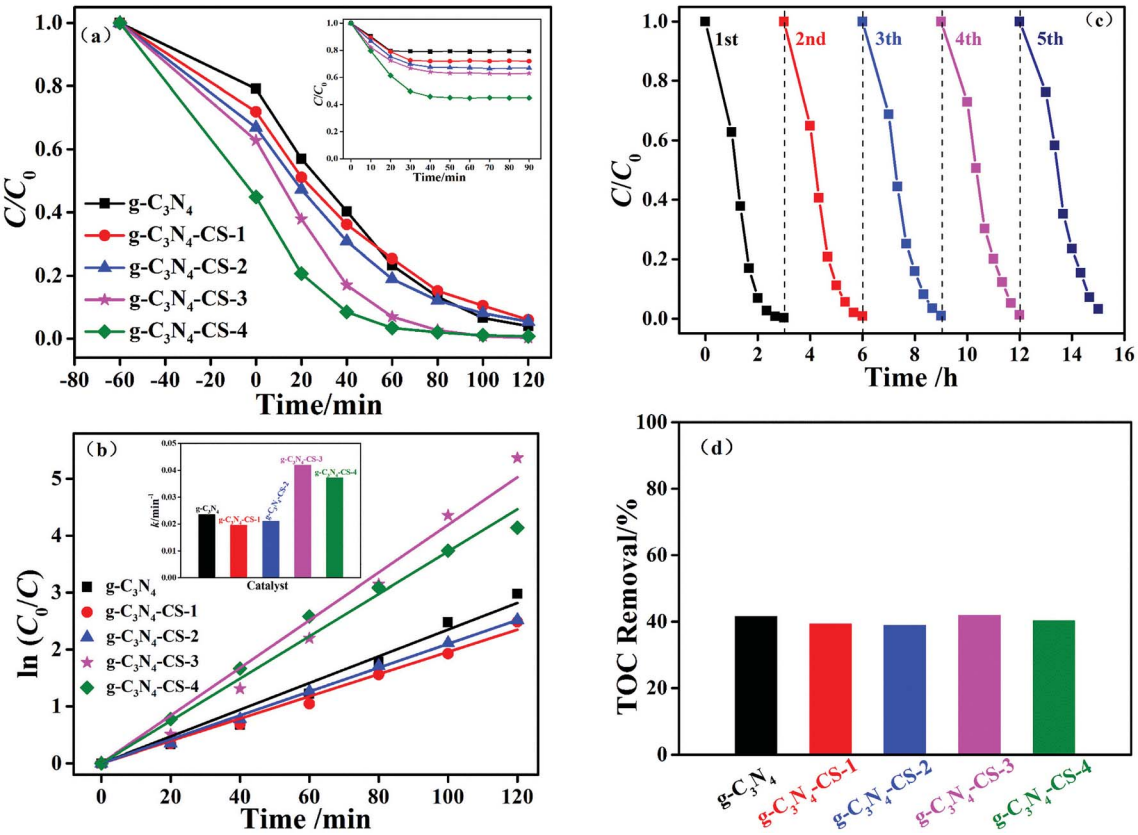

Fig. 10 (a) Photocatalytic degradation of MB over the g-C_3N_4 and g-C_3N_4–CS-x photocatalysts under visible light irradiation, where the inset is the adsorption–desorption equilibrium curves in the dark; and (b) the corresponding first-order-kinetic plots, where the inset shows the corresponding rate constants. (c) The stability test of g-C_3N_4–CS-3 under visible light irradiation. (d) TOC removal of the g-C_3N_4 and g-C_3N_4–CS-x photocatalysts under visible light irradiation.

$$\ln(C_0/C) = kt \quad (1)$$

where k is the apparent first-order rate constant (min^{-1}), t is the illumination time (min), C_0 is the initial concentration of the solution, and C is the concentration at reaction time t under illumination. The inset is the corresponding rate constants showing that the first-order reaction kinetic constant of the g-C_3N_4–CS-3 beads is higher than those of the others by a factor of 1.78 (Fig. 10b).

The stability of the optimized g-C_3N_4–CS-3 beads was tested for five consecutive cycles under illumination by visible light (Fig. 10c). The sample activities decreases slightly after five repeat reaction cycles under the same experimental conditions, which may be because after several photocatalytic degradations, the active sites of the catalyst were reduced. However, after five times of repeated use, the degradation rate can still reach approximately 97%, and the mass change does not exceed 10%. The above data show that the g-C_3N_4–CS-3 beads have high stability and can meet the needs of practical application.

The removal efficiency of TOC by g-C_3N_4 and g-C_3N_4–CS-x photocatalysts can reached about 40% (Fig. 10d). The removal rate of g-C_3N_4–CS-3 is relatively high could be attributed to the synergetic effect between the adsorption of CS and photocatalytic activity of g-C_3N_4.

To research the possible mechanism of the photolysis performance, we identify the active species by adding radical scavengers, with BQ as the $\cdot O_2^-$ scavenger,[51] IPA as the $\cdot$OH scavenger,[37] and TEOA as the hole (h^+) scavenger,[52] during the photocatalytic degradation process. As shown in Fig. 11, the photocatalytic activity of the g-C_3N_4–CS-3 beads substantially

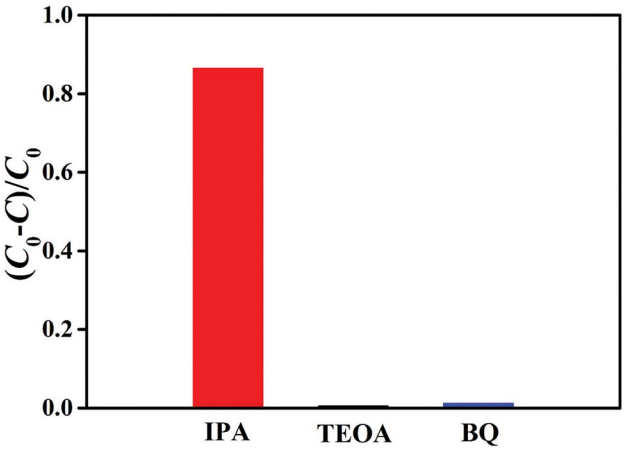

Fig. 11 Photodegradation rates of MB over the g-C_3N_4–CS-3 beads in the presence of different scavengers.

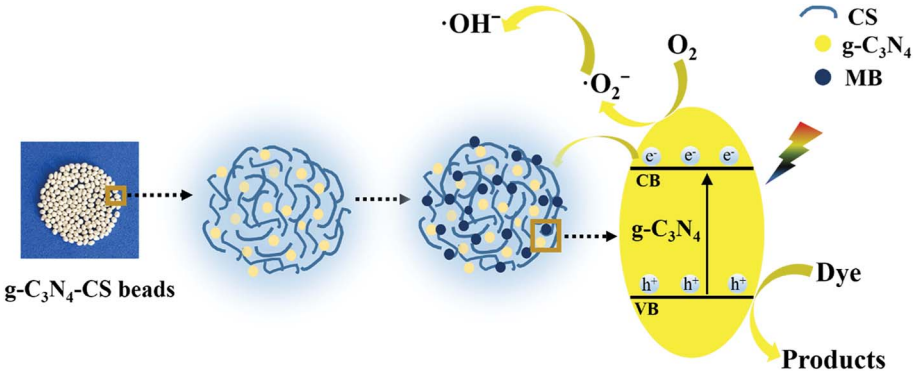

Fig. 12 The possible mechanism of the g-C_3N_4–CS beads under visible light.

decreased when TEOA and BQ were added, which indicates that h^+ and $\cdot O_2^-$ are the main active species in the process, respectively. The photocatalytic activity decreased slightly when IPA was dispersed into the aqueous solution. Thus, the influence order of the activated species in the process of MB photodegradation is $h^+ > \cdot O_2^- > \cdot OH$.

From the above, the possible mechanism of the g-C_3N_4–CS beads is shown in Fig. 12. Photo-generated electrons migrate from the valence band (VB) to the conduction band (CB) under visible light irradiation, the holes can oxidize dyes to products such as CO_2 and H_2O, and the electrons can reduce O_2 to $\cdot O_2^-$ and further react to produce ·OH. At the same time, it is unknown whether electrons can be transferred from the conduction band (CB) to CS, which need further experiments to prove.

4. Conclusions

In summary, we have successfully fabricated the regenerable g-C_3N_4–CS beads *via* the blend crosslinking method. The mass ratio of g-C_3N_4 to CS had an important influence on the photocatalytic activity toward *in situ* adsorption and decomposition MB under visible light irradiation. At the optimal g-C_3N_4 content, the as-prepared g-C_3N_4–CS-3 sample exhibited the highest photocatalytic performance, exceeding that of pure g-C_3N_4 by a factor of 1.78. The enhanced photocatalytic performance was ascribed to the synergistic effect between *in situ* adsorption and photocatalytic degradation. The active species trapping experimental results demonstrated that the superoxide radicals ($\cdot O_2^-$) and holes (h^+) were the main active species in the decomposition of MB. In addition, the reacted g-C_3N_4–CS beads can be regenerated by merely adding sodium hydroxide and hydrogen peroxide with a mass loss of less than 10% in recycles. This work might provide new insight for the smart design and fabrication of highly efficient regenerated g-C_3N_4-based photocatalysts for environmental purification.

Conflicts of interest

The authors declare that there is no conflict of interest.

Acknowledgements

The authors are grateful for the financial support from the National Science and Technology Major Project (NO. 2016ZX05040003) and the Fundamental Research Funds for the Central Universities (NO. 17CX06027, NO. 18CX06068A).

References

1 Z. Dong and Y. Wu, *J. Photochem. Photobiol., A*, 2017, **336**, 156–163.
2 P. Djinović and A. Pintar, *Appl. Catal., B*, 2017, **206**, 675–682.
3 S. Ye, L.-G. Qiu, Y. P. Yuan, Y. J. Zhu, J. Xia and J. F. Zhu, *J. Mater. Chem. A*, 2013, **1**, 3008.
4 D. Masih, Y. Ma and S. Rohani, *Appl. Catal., B*, 2017, **206**, 556–588.
5 H. Lin, Y. Liu, J. Deng, S. Xie, X. Zhao, J. Yang, K. Zhang, Z. Han and H. Dai, *J. Photochem. Photobiol., A*, 2017, **336**, 105–114.
6 Y. Liu, W. Jin, Y. Zhao, G. Zhang and W. Zhang, *Appl. Catal., B*, 2017, **206**, 642–652.
7 H. Sun, G. Zhou, Y. Wang, A. Suvorova and S. Wang, *ACS Appl. Mater. Interfaces*, 2014, **6**, 16745–16754.
8 P. Liang, C. Zhang, H. Sun, S. Liu, M. Tadé and S. Wang, *RSC Adv.*, 2016, **6**, 95903–95909.
9 D. Dvoranová, M. Mazúr, I. Papailias, T. Giannakopoulou, C. Trapalis and V. Brezová, *Catalysts*, 2018, **8**, 47.
10 Z. Zhu, M. Murugananthan, J. Gu and Y. Zhang, *Catalysts*, 2018, **8**, 112.
11 S. Halevy, E. Korin and A. Bettelheim, *RSC Adv.*, 2016, **6**, 87314–87318.
12 W. Zhang, Z. Zhang, S. Kwon, F. Zhang, B. Stephen, K. K. Kim, R. Jung, S. Kwon, K.-B. Chung and W. Yang, *Appl. Catal., B*, 2017, **206**, 271–281.
13 H. Li, T. Hu, R. Zhang, J. Liu and W. Hou, *Appl. Catal., B*, 2016, **188**, 313–323.
14 L. Zhang, X. He, X. Xu, C. Liu, Y. Duan, L. Hou, Q. Zhou, C. Ma, X. Yang, R. Liu, F. Yang, L. Cui, C. Xu and Y. Li, *Appl. Catal., B*, 2017, **203**, 1–8.
15 Y. He, M. E. Ford, M. Zhu, Q. Liu, Z. Wu and I. E. Wachs, *Appl. Catal., B*, 2016, **188**, 123–133.

16 Y. Cui, Q. Ma, X. Deng, Q. Meng, X. Cheng, M. Xie, X. Li, Q. Cheng and H. Liu, *Appl. Catal., B*, 2017, **206**, 136–145.
17 Z. Bian, J. Zhu, F. Cao, Y. Huo, Y. Lu and H. Li, *Chem. Commun.*, 2010, **46**, 8451–8453.
18 S. Sun, J. Zhang, P. Gao, Y. Wang, X. Li, T. Wu, Y. Wang, Y. Chen and P. Yang, *Appl. Catal., B*, 2017, **206**, 168–174.
19 X. H. Yang, Z. Li, C. Sun, H. G. Yang and C. Li, *Chem. Mater.*, 2011, **23**, 3486–3494.
20 S. Khan, H. Cho, D. Kim, S. S. Han, K. H. Lee, S. H. Cho, T. Song and H. Choi, *Appl. Catal., B*, 2017, **206**, 520–530.
21 X. Bai, L. Wang, R. Zong and Y. Zhu, *J. Phys. Chem. C*, 2013, **117**, 9952–9961.
22 J. Jiang, S. Cao, C. Hu and C. Chen, *Chin. J. Catal.*, 2017, **38**, 1981–1989.
23 J. Fu, J. Yu, C. Jiang and B. Cheng, *Adv. Energy Mater.*, 2018, **8**, 1701503.
24 X. Chen, Y.-S. Jun, K. Takanabe, K. Maeda, K. Domen, X. Fu, M. Antonietti and X. Wang, *Chem. Mater.*, 2009, **21**, 4093–4095.
25 X. Wang, X. Chen, A. Thomas, X. Fu and M. Antonietti, *Adv. Mater.*, 2009, **21**, 1609–1612.
26 L. Zhou, H. Zhang, X. Guo, H. Sun, S. Liu, M. O. Tade and S. Wang, *J. Colloid Interface Sci.*, 2017, **493**, 275–280.
27 K. C. Christoforidis, M. Melchionna, T. Montini, D. Papoulis, E. Stathatos, S. Zafeiratos, E. Kordouli and P. Fornasiero, *RSC Adv.*, 2016, **6**, 86617–86626.
28 A. H. Reshak, S. A. Khan and S. Auluck, *RSC Adv.*, 2014, **4**, 11967–11974.
29 A. Akhundi and A. Habibi-Yangjeh, *RSC Adv.*, 2016, **6**, 106572–106583.
30 Y. Zhao, X. Liang, Y. Wang, H. Shi, E. Liu, J. Fan and X. Hu, *J. Colloid Interface Sci.*, 2018, **523**, 7–17.
31 Z. Zhang, Y. Zhang, L. Lu, Y. Si, S. Zhang, Y. Chen, K. Dai, P. Duan, L. Duan and J. Liu, *Appl. Surf. Sci.*, 2017, **391**, 369–375.
32 S. Sahar, A. Zeb, Y. Liu, N. Ullah and A. Xu, *Chin. J. Catal.*, 2017, **38**, 2110–2119.
33 Y. Xu, H. Xu, L. Wang, J. Yan, H. Li, Y. Song, L. Huang and G. Cai, *Dalton Trans.*, 2013, **42**, 7604–7613.
34 J. Wang, Y. Xia, H. Zhao, G. Wang, L. Xiang, J. Xu and S. Komarneni, *Appl. Catal., B*, 2017, **206**, 406–416.
35 E. Fayyad, A. Abdullah, M. Hassan, A. Mohamed, C. Wang, G. Jarjoura and Z. Farhat, *Coatings*, 2018, **8**, 37.
36 S. A. Younis, A. Abd-Elaziz and A. I. Hashem, *RSC Adv.*, 2016, **6**, 89367–89379.
37 Y. Wang, H. Wang, F. Chen, F. Cao, X. Zhao, S. Meng and Y. Cui, *Appl. Catal., B*, 2017, **206**, 417–425.
38 J. Fu, B. Zhu, C. Jiang, B. Cheng, W. You and J. Yu, *Small*, 2017, **13**, 1603938.
39 L. Zhou, H. Zhang, H. Sun, S. Liu, M. O. Tade, S. Wang and W. Jin, *Catal. Sci. Technol.*, 2016, **6**, 7002–7023.
40 K. V. Harish Prashanth and R. N. Tharanathan, *Carbohydr. Res.*, 2006, **341**, 169–173.
41 L. Zhou, Z. Liu, J. Liu and Q. Huang, *Desalination*, 2010, **258**, 41–47.
42 J. Berger, M. Reist, J. M. Mayer, O. Felt, N. A. Peppas and R. Gurny, *Eur. J. Pharm. Biopharm.*, 2004, **57**, 19–34.
43 P. Xu, X. Liang, N. Chen, J. Tang, W. Shao, Q. Gao and Z. Teng, *J. Colloid Interface Sci.*, 2017, **507**, 353–359.
44 P. A. Nishad, A. Bhaskarapillai and S. Velmurugan, *Carbohydr. Polym.*, 2014, **108**, 169–175.
45 L. Yang, L. Jiang, D. Hu, Q. Yan, Z. Wang, S. Li, C. Chen and Q. Xue, *Carbohydr. Polym.*, 2016, **140**, 433–441.
46 X. J. Wang, C. Liu, X. L. Li, F. T. Li, Y. P. Li, J. Zhao and R. H. Liu, *Appl. Surf. Sci.*, 2017, **394**, 340–350.
47 Y. Lu, C. Ji, Y. Li, R. Qu, C. Sun and Y. Zhang, *Mater. Lett.*, 2018, **211**, 78–81.
48 Z. Ji, Z. Shengtang, W. Guangpeng, W. Wenqiang, G. Sufang, Z. Ji and W. Yunpu, *J. Bioact. Compat. Polym.*, 2016, **22**, 429–441.
49 I. F. Amaral, P. L. Granja and M. A. Barbosa, *J. Biomater. Sci., Polym. Ed.*, 2005, **16**, 1575–1593.
50 R. S. Vieira, M. L. M. Oliveira, E. Guibal, E. Rodríguez-Castellón and M. M. Beppu, *Colloids Surf., A*, 2011, **374**, 108–114.
51 B. Chai, J. Yan, C. Wang, Z. Ren and Y. Zhu, *Appl. Surf. Sci.*, 2017, **391**, 376–383.
52 B. Wang, J. Di, P. Zhang, J. Xia, S. Dai and H. Li, *Appl. Catal., B*, 2017, **206**, 127–135.